

# Quantum delocalization of a 1-milligram torsional pendulum for gravity experiments

Sofia Agafonova<sup>1</sup>, Pere Rossello<sup>1</sup>, Manuel Mekonnen<sup>1</sup>, Onur Hosten<sup>1\*</sup>,

<sup>1</sup>Institute of Science and Technology Austria, Klosterneuburg, Austria.

**Reconciling gravity and quantum mechanics has posed significant challenges in contemporary physics. Even the seemingly simple question of whether gravitational fields should obey the quantum superposition principle remains unanswered. Unlocking the answer experimentally necessitates a quantum-unfriendly regime with large masses and low-frequency dynamics to maximize the dimensionless figure-of-merit in the problem, quantifying the ability to generate quantum entanglement gravitationally. To this end, we develop a 1-milligram torsional pendulum operating at 18 Hz. Laser cooling its motion to an unprecedented 240 microkelvins for this mass range, we boost its quantum delocalization and benchmark a state-of-the-art quantum-gravity figure-of-merit with an unparalleled improvement potential. The results open a frontier for explorations of quantum aspects of gravity, establishing milligram-scale torsional pendulums as a leading platform.**

All known fundamental interactions, except gravity, have been verified to obey the laws of quantum mechanics. Theoretically, reconciling gravity with quantum mechanics has proven challenging to the level that inspired many attempts to alternative theories where gravity remains fundamentally non-quantum (1) — reference (2) is an example of a consistent one. Experimentally, the situation is only bleaker: to date, no experiment has reached a regime in which the gravitational interactions of two objects that behave quantum-mechanically dictate the dynamics. In this regime, quantum uncertainties in the position of a mechanical object — the quantum delocalization — lead to

quantum uncertainties in the gravitational fields sourced (3). Currently, the most concrete idea for testing whether gravity needs a quantum description is to test whether gravitational interactions between objects can generate quantum entanglement (4, 5). Such tests will allow us to get a first glimpse at the putative quantum nature of gravitational fields.

Whereas femto-to-microgram-scale oscillators allowed observation of quantum mechanics in macroscopic objects (6), and gram-to-ton-scale oscillators enabled exploration of gravitational wave detection (7); the microgram-to-milligram scale (8–17) is arguably the sweet spot to probe the quantum-gravity interface. The reasons are simple: Quantum control is challenging with larger objects, while significant gravitational interaction is difficult with smaller objects. The feasibility of such experiments is not unwarranted with today’s technology, but the challenges are demanding (18). The current race to develop technologies that will realize the required leaps will result in not only notable advances in the direction of gravity-mediated entanglement, but also in the study of optomechanical entanglement (19, 20), quantum decoherence (21, 22), semi-classical gravity models (23), spontaneous wave function collapse (24), the nature of dark matter (25), and deviations from Newtonian / Einsteinian gravity (26, 27).

Gravitational entanglement between two objects can be generated by two seemingly distinct procedures. In one case (4, 5), each of the masses can be placed in a quantum superposition with wavepacket separation  $\xi$  to run a pair of matter wave interferometers separated by a larger center distance  $d$ . Alternatively (28–32), the quantum state of each of the masses can be prepared in a coherent Gaussian wavepacket of spatial spread  $\xi$  — a continuum of superpositions — with the two masses separated by  $d$ . In either case, depending on their quantum delocalizations  $\xi$ , the masses are expected to develop quantum entanglement at a rate proportional to the inter-mass force gradient  $|\nabla F|$  (18, 29, 30, 33). For example, for two point particles with mass  $m$  each,  $|\nabla F| = 2Gm^2/d^3$ , where  $G$  is the gravitational constant. For two gravitationally coupled oscillators with angular frequencies  $\omega_0$ , the dimensionless number

$$\eta^2 = \frac{\xi^2 |\nabla F|}{\hbar \omega_0} \quad (1)$$

quantifies the amount of entanglement generated in one oscillation cycle at zero temperature —  $\hbar$ : reduced Planck constant,  $\eta^2 = 1$ : significant entanglement in a fraction of a cycle. The definition of this quantity follows reference (29), but leaves the experimentally tunable quantum delocalization

$\xi$  and the force gradient  $|\nabla F|$  explicit — instead of inserting oscillator zero-point fluctuations  $x_{zp} \equiv \sqrt{\hbar/2m\omega_0}$  and point-particle force gradients. For a single oscillator, we can universally define  $\eta$  as the figure-of-merit for its utility for experiments at the quantum-gravity interface. We draw attention to this quantity for the first time from an experimental perspective.

The use of entanglement generation per cycle — instead of entanglement rate — enables a meaningful comparison of a wide range of oscillators, since detrimental dissipative effects universally dilute as physical oscillator periods become longer (10). The effectiveness of low-frequency oscillators for entanglement generation enters  $\eta$  both explicitly through the  $\omega_0$  denominator and implicitly through the achievable quantum delocalization. The ability to readily compare many existing systems for their quantum delocalization  $\xi$  stems from the lack of a clear boundary between the classical and quantum worlds: For a rigorous definition of quantum delocalization  $\xi$ , we will use the object’s *quantum coherence length*, first developed in ref. (34), corresponding to the spatial distance over which the object can show quantum interference effects. In this context, for an oscillator in a thermal state, a characterized temperature  $T$  is a witness for its quantum delocalization  $\xi = x_{zp}/\sqrt{(2n+1)}$ , where  $n$  is the mean thermal excitation number (Supplementary Text). Note that unlike the overall position uncertainty  $\Delta x = x_{zp}\sqrt{2n+1}$ , which increases with temperature,  $\xi$  instead shrinks.

In this work, we develop the first generation of an experiment aiming to achieve a large figure of merit  $\eta$  for the experimental quantum-gravity interface by developing and manipulating a 1-milligram suspended torsional pendulum. We demonstrate laser cooling of the pendulum motion through radiation-pressure feedback, suppressing the thermal motion from room temperature to an effective temperature of 240  $\mu\text{K}$ , extending the objects coherence length. Cooling is achieved by first optically trapping the torsional motion to shift its frequency from 6.72 Hz to 18.0 Hz, and then by critically damping the motion. With the developed system, we benchmark an experimentally spearheading quantum-gravity figure-of-merit  $\eta = 2.8 \times 10^{-9}$  that we will put into context below. In addition to this main result, the achieved cooling levels significantly surpass the lowest reported motional temperatures in the microgram-to-kilogram mass window — 6 mK for the gram scale (35) and 15 mK for the milligram scale (36) — and the achieved torque sensitivity of  $1.2 \times 10^{-18} \text{N}\cdot\text{m}/\sqrt{\text{Hz}}$  constitute a record value for the milligram scale – a factor of 10 beyond reference (14).

## Setup

The pendulum used in this study is shown in Figure 1A inside its vacuum housing maintained at  $5 \times 10^{-9}$ -mbar. The pendulum consists of a  $2 \times 0.5 \times 0.5 \text{ mm}^3$  silver-coated fused silica mirror bar, and a  $10\text{-}\mu\text{m}$  diameter fused silica suspension fiber of 5-cm length. It exhibits a torsional (yaw) resonance at  $f_0 \equiv \omega_0/2\pi = 6.72 \text{ Hz}$  in addition to longitudinal and transverse swing modes at  $2.27 \text{ Hz}$ , a roll mode at  $44.48 \text{ Hz}$ , and a pitch mode at  $125.95 \text{ Hz}$  (Fig. 1A, overlay). The piece used for the pendulum bar was cut from a larger optical mirror, and the suspension fiber was manufactured in-house from a standard  $125\text{-}\mu\text{m}$ -diameter optical fiber (S630-HP) by wet etching. The etching process was designed to leave  $500 \mu\text{m}$  long tapers at both ends (Fig. 1A, inset) to allow adhesive-aided attachment without introducing mechanical losses. In this way, the torsional energy is mainly stored in the high-compliance thin section of the fiber, preventing dissipation at the low-compliance  $125\text{-}\mu\text{m}$  diameter adhesive-bonded (Norland 61) surfaces. This design achieves a quality factor of  $Q_0 = \tau\omega_0/2 = 8.6 \times 10^4$  for the yaw mode, as measured by a ring-down of its oscillation amplitude with a time constant of  $\tau = 4058 \text{ s}$  (Fig. 1D). The ring-down thermally equilibrates around  $(k_B T_0 / (I\omega_0^2))^{1/2} = 2.6 \mu\text{rad}$  fluctuations dictated by the equipartition theorem. Here; moment of inertia  $I = 3.3 \times 10^{-13} \text{ kg} \cdot \text{m}^2$ , ambient temperature  $T_0 = 295 \text{ K}$ , Boltzmann's constant  $k_B$ . The measured  $Q_0$  and the corresponding mechanical energy dissipation rate of  $\gamma_0 = \omega_0/Q_0 = 2\pi \times 79 \mu\text{Hz}$  indicate excellent performance even compared to monolithic pendulums manufactured with laser-welded suspensions (10) — with room only for a factor of 2-3 improvement given standard material loss limitations for the utilized fiber's surface-to-volume ratio (38).

The near-ideal thermally-limited noise spectrum (Fig. 1C) reveals that dissipation in the yaw motion arises purely from structural damping, with no observable viscous contribution from background gas. This spectrum arises from a thermal (th) torque ( $\tau$ ) noise of power spectral density (PSD)  $S_{\tau\tau}^{th} = 4k_B T_0 I \gamma(\omega)$  with frequency-dependent structural dissipation rate  $\gamma(\omega) = \gamma_0 \frac{\omega_0}{\omega}$  (17). The torque noise manifests itself as an angular ( $\theta$ ) PSD  $S_{\theta\theta}^{th} = |\chi|^2 S_{\tau\tau}^{th}$  through the mechanical susceptibility  $\chi(\omega) = (\omega_0^2 - \omega^2 + i\omega\gamma(\omega))^{-1}/I$ , showing excellent agreement with the measurements. The agreement in the peak region (Fig. 1C, inset) indicates a resonance frequency instability below  $100 \mu\text{Hz}$ . The minimal observed torque noise of  $1.2 \times 10^{-18}$ , makes the system excel as a

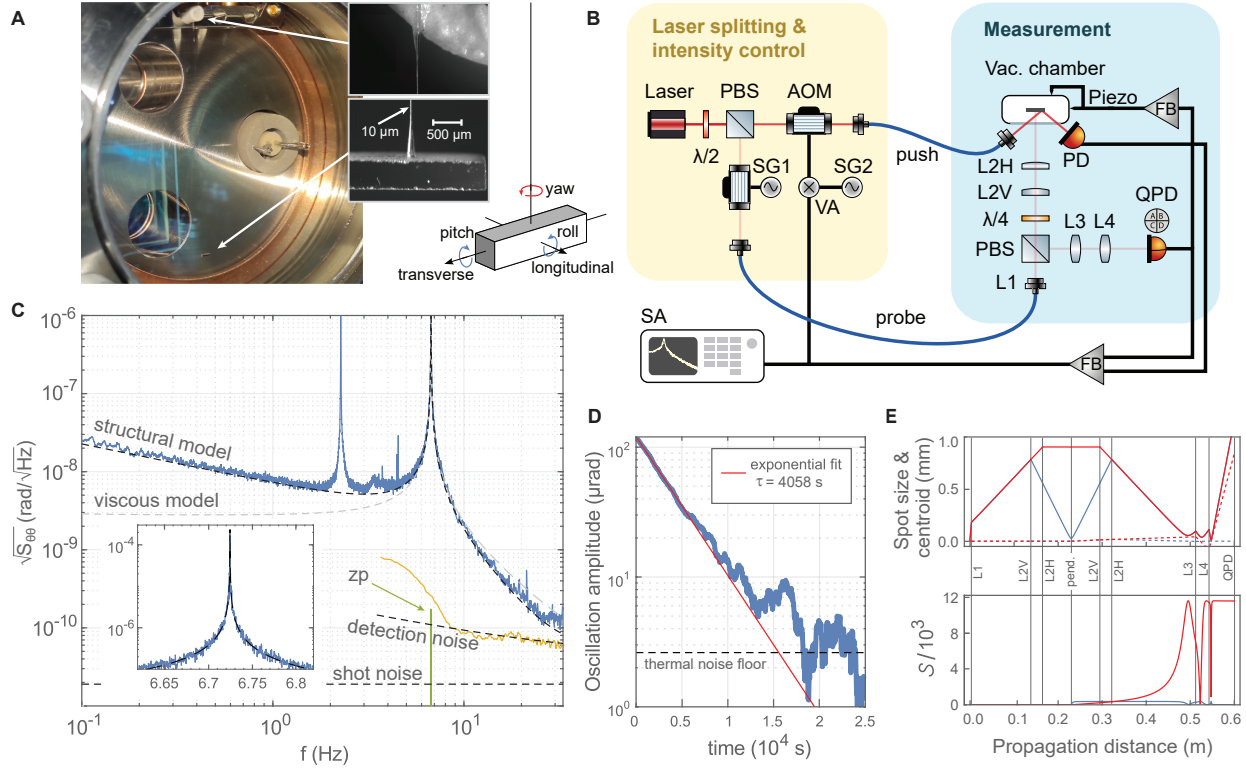


**Figure 1: Experimental setup and its characterization.** (A) Photo of the pendulum inside the vacuum chamber. Insets: Tapered suspension fiber ends and the pendulum mirror bar. Overlay: Definitions of pendulum modes. (B) Schematics of the optical setup. PBS: polarizing beam splitter,  $\lambda/2$ : half-wave plate,  $\lambda/4$ : quarter-wave plate, AOM: acousto-optic modulator, SG: signal generator, VA: variable attenuator, SA: digitization and spectrum analysis, FB: feedback circuit, PD: photodetector, QPD: quadrant photodetector, L2H(V): horizontal (vertical) cylindrical lens with 200 mm (60 mm) focal length, L1(3, 4): spherical lens with 4.5 mm (10 mm, 4.0 mm) focal length. (C) Steady-state yaw noise spectrum (blue) compared to thermal noise models (dashed lines) with structural or viscous damping. Inset: close-up of the resonance peak, orange data: detection noise spectrum compared to theoretical laser shot-noise (37), “zp” curve: theoretical spectrum for quantum zero-point fluctuations associated with the yaw motion for reference. The parasitic 2.27-Hz peak is due to the residual swing motion sensitivity in the yaw channel. The “detection noise” model incorporates a variable “white +  $1/f$ ” noise to fit the data above 8 Hz. (D) Ring-down measurement of the 6.72-Hz yaw oscillations. (E) Implemented probe beam profile across the lens system for horizontal (red) and vertical (blue) directions. Top; solid lines: beam spot size evolution, dashed lines: beam centroid evolution for a 100- $\mu$ rad illustrative yaw (red) or pitch (blue) rotation of the pendulum. Bottom; evolution of the tilt sensitivity parameter  $\mathcal{S}$ .

competitive sensor; see (39) for details.

The characterization of the motion is enabled by an optical lever capable of resolving the motion at the level of quantum zero-point fluctuations  $S_{\theta\theta}^{zP} = S_{\theta\theta}^{th}/(2n_0 + 1)$  that would be associated with the yaw oscillations (Fig. 1C). Here,  $n_0 \approx k_B T_0 / \hbar \omega_0 = 9.2 \times 10^{11}$  is the mean number of thermal excitation quanta. The calibration of the optical lever signal was done by replacing the pendulum with a rigid rotatable mirror. Based on this calibration, the measured yaw angle noise agrees with the expected thermal noise levels to within 10%. The detection noise spectrum shown in Figure 1C is the base noise of the optical lever obtained in this rigid mirror configuration.

The optical setup around the pendulum is shown in Figure 1B. The output of a 780-nm DFB laser is split into two paths: one to probe the pendulum's motion (10  $\mu$ W) and the other to manipulate it through radiation pressure (0-4 mW). Acousto-optic modulators (AOM) enable intensity control on each path. The Gaussian probe beam is incident at the center of the pendulum, and circulates back to a quadrant photodiode (QPD), which reads the horizontal and vertical positions of the beam to yield the pendulum motion.

An arrangement of cylindrical and spherical lenses maximizes the sensitivity to yaw motion (horizontal beam tilt), while minimizing the sensitivity to any type of mechanical mode that leads to a pitching-like motion (vertical beam tilt). The beam shaping principle is based on two considerations (39): 1) independently of beam divergence, the fundamental tilt sensitivity is linearly proportional to the beam spot size  $w_p$  at the pendulum, and 2) the utilized tilt sensitivity parameter  $\mathcal{S} = \sqrt{\frac{8}{\pi}} \frac{d}{d\theta} \frac{\delta(\theta)}{w}$  ( $\text{rad}^{-1}$ ) can be maximized to  $\mathcal{S}_{\text{max}} = \frac{\sqrt{32\pi}}{\lambda} w_p$  for any desired beam size at the detection point, extracting the tilt information optimally. In the definition of the sensitivity parameter,  $w$  and  $\delta(\theta)$  are the spot size and the tilt-induced beam displacement at the detection point; and  $\lambda$  is the wavelength. With these definitions, the quantity  $1/(\mathcal{S} \theta)^2$  has the interpretation of the total number of photons required for the QPD to resolve a pendulum tilt  $\theta$ . The implemented probe beam profile and the sensitivity  $\mathcal{S}$  as a function of detection distance are illustrated in Figure 1E.  $\mathcal{S}$  is maximized in the horizontal channel and minimized in the vertical one, both for a large spot size at the detection point, avoiding photodiode gaps.

The QPD output is fed into a home-built analog feedback circuit to control the push beam power incident on the corner of the pendulum to implement effective equations of motion for the yaw mode (Fig. 1B). Although the detection is optimized for the yaw motion, smaller signals from all

other modes of the pendulum are also available on the QPD output. We use these to dampen those other modes via feedback by pushing on the vacuum chamber with piezo-actuators (39).

## Optomechanical control

The feedback-based radiation forces are designed to implement the effective susceptibility function

$$\chi_{\text{eff}}(\omega) = (\omega_{\text{eff}}^2 - \omega^2 + i\omega\gamma_{\text{eff}})^{-1}/I \quad (2)$$

of a torsional harmonic oscillator with tunable frequency and damping. The analog feedback circuit implementing the effective susceptibility contains two key parameters: gain of the feedback loop  $g$  and the lead-filter corner frequency  $\omega_{\text{lead}}$ . Physically, while the gain controls the strength of the applied restoring torque, the lead filter introduces the time derivative of the measured yaw angle, implementing velocity damping (39). The parameters dictate the effective resonance frequency  $\omega_{\text{eff}} = \omega_0\sqrt{1+g}$  and the effective damping rate  $\gamma_{\text{eff}} = \frac{\omega_0^2 g}{\omega_{\text{lead}}} + \gamma(\omega)$ . Here, the intrinsic damping  $\gamma(\omega)$  is negligible relative to the feedback damping term, rendering the effective damping independent of frequency (purely viscous) with an effective quality factor of  $Q_{\text{eff}} = \frac{\omega_{\text{eff}}}{\gamma_{\text{eff}}}$ .

Figure 2A illustrates our ability to shift the torsional oscillation frequency through feedback-based optical forces, realizing an optical torsion spring. To experimentally characterize the effective susceptibilities, we optically apply a white-noise torque drive to the pendulum that is about 100 times the thermal torque noise. This creates a large motion, enabling an easy measurement of the angular noise spectrum to calculate  $|\chi_{\text{eff}}| = (S_{\theta\theta}/S_{\tau\tau})^{1/2}$ . During these measurements, we additionally induce a level of feedback-damping to stay below the maximal restoring torque that can be supplied by the finite power of the push beam. For each configuration, the effective frequencies and quality factors are extracted by fitting Eq. 2 to the data, obtaining excellent agreement with the intended effective susceptibilities.

Unlike the restoring torsion provided by the suspension fiber that brings in thermal torque noise, the optically induced torques can practically be noise-free (40). An oscillator whose frequency is increased by an optical spring acquires a new set of *apparent* parameters that dictate its properties. Defining the *apparent* quantities for the case of ‘no induced feedback damping’, the susceptibility describing the oscillator becomes  $\chi_{\text{app}}(\omega) = (\omega_{\text{eff}}^2 - \omega^2 + i\omega\gamma(\omega))^{-1}/I$ , where  $\gamma(\omega)$  is the original structural damping function. The resonant damping rate decreases to  $\gamma_{\text{app}} = \gamma(\omega_{\text{eff}}) = \gamma_0 \frac{\omega_0}{\omega_{\text{eff}}}$ , and

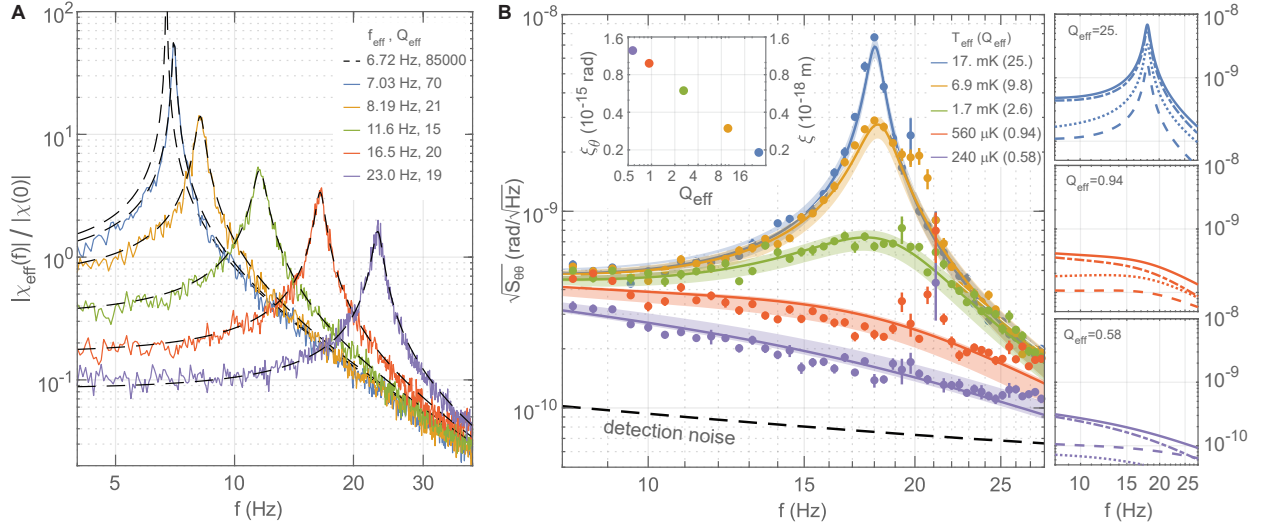


**Figure 2: Feedback control of the motion, temperatures, coherence lengths (A)** Experimental effective susceptibilities as the resonance frequency of the pendulum is shifted under feedback control. Normalization is to the DC value of the feedback-free susceptibility. **(B)** Noise spectral densities for different feedback damping strengths for the pendulum shifted to 18 Hz. Data points: mean spectral density within each 2.4-Hz frequency bin, error bars:  $\pm 1$  standard deviation within each bin, solid lines: theoretical noise models with excess vibration noise as a fit parameter, error bands: variation in the model curves due to the full-range of lab vibration noise level changes, detection noise: same as Fig. 1. Inset: coherence angles  $\xi_{\theta}$  and pendulum-tip coherence lengths  $\xi$ . Side panels show the noise breakdown for representative damping strengths. Solid lines: total noise, dash-dotted lines: theoretical thermal noise given the effective susceptibilities, dashed lines: theoretical imprinted measurement noise, dotted lines: extracted white-torque-noise equivalent vibration noise.

the resonant quality factor increases to

$$Q_{\text{app}} = \frac{\omega_{\text{eff}}}{\gamma_{\text{app}}} = Q_0 \left( \frac{\omega_{\text{eff}}}{\omega_0} \right)^2. \quad (3)$$

The larger the apparent quality factor, the more the oscillator can be cooled. To understand this, note that feedback cooling sets the value of  $\gamma_{\text{eff}}$  in Eq. 2, reducing the resonance peak height without adding noise. The largest meaningful value of  $\gamma_{\text{eff}}$  is achieved at critical damping  $Q_{\text{eff}} = 1/2$ , after which point there is no oscillator. Therefore, one needs to start with a high quality factor to be able to achieve large cooling factors.

To explore the limits of our ability to cool the yaw motion, we shift the yaw-mode resonance to 18 Hz, to the center of the excess-noise-free frequency band from 8 to 28 Hz. Below 8 Hz, spurious detection noise kicks in; above 28 Hz, excess noise of the 44-Hz roll motion leaks into the yaw-angle measurement. For the 18-Hz oscillator, the apparent quality factor is  $Q_{\text{app}} = 6.1 \times 10^5$ . After shifting the frequency, we implement five different feedback circuit configurations with effective damping rates corresponding to quality factors ranging from  $Q_{\text{eff}} = 25$  to  $Q_{\text{eff}} = 0.58$ . We characterize the resulting effective susceptibilities using the same procedure described in the context of Figure 2A. Then, for each feedback configuration, we let the system operate without any external driving torque. Figure 2B shows the yaw motion noise spectra obtained, showing the progressively colder oscillator states.

The resulting motion is governed by the conversion of three torque noise contributions to angular motion: structural thermal noise, detection noise that is imprinted on the motion through the feedback loop, and vibrations that affect the yaw motion (see (39) for model details). Given the theoretical thermal noise, the characterized susceptibilities, and the detection noise, the only unknown is the vibration noise in the system — known to be nonstationary. We take the vibration spectra to be approximately white noise (in torque) within the frequency band of interest and set its amplitude to be the fit parameter for the overall model. The resulting model curves are shown together with the spectral noise data in Figure 2B. The noise breakdown is illustrated in the right panel of Figure 2B as well for exemplary cases: the system is driven dominantly by thermal noise, while the imprinted measurement noise and vibration noise are always subdominant.

The extent of the fluctuations in the yaw angle  $\theta$  around zero can be expressed as an effective temperature  $T_{\text{eff}} = I\omega_{\text{eff}}^2 \langle \theta^2 \rangle / k_B$  for this motion. In this context, the yaw angle fluctuations are

determined by the integral of the angular PSD:  $\langle \theta^2 \rangle = \int_0^\infty S_{\theta\theta}(f) df$ . The value of this integral is dominated by the contributions within the vicinity of the resonance peak. In fact, under the action of thermal noise alone, taking the PSD for the case of a purely frequency-shifted pendulum  $S_{\theta\theta}^{\text{app}} = |\chi_{\text{app}}|^2 S_{\tau\tau}^{\text{th}}$ , one recovers to a good approximation the equipartition theorem  $I\omega_{\text{eff}}^2 \langle \theta^2 \rangle_{\text{app}} = k_B T_0$  (40, 41) — already reaching to a 94% accuracy even within a small integration band of  $10 \frac{\gamma_{\text{app}}}{2\pi} \equiv 0.29$  mHz. Experimentally, the achieved effective temperatures can be determined by referencing the observed angular fluctuations within the accessible observation band to those of the ideal frequency-shifted oscillator:

$$\frac{T_{\text{eff}}}{T_0} = \frac{\int_{f_1}^{f_2} S_{\theta\theta}(f) df}{\int_{f_1}^{f_2} S_{\theta\theta}^{\text{app}}(f) df}. \quad (4)$$

In our case,  $f_1 = 8$  Hz and  $f_2 = 28$  Hz. For each damping configuration in Figure 2B, the temperatures extracted using Eq. 4 are indicated, reaching a minimum of  $238 \pm 8$   $\mu\text{K}$  near critical damping. The uncertainty represents the 95% confidence range of the model fit. This temperature is equivalent to a mean thermal excitation quanta of  $n = 2.8 \times 10^5$ .

## Putting into context

We now return to the figure-of-merit  $\eta$  (Eq. 1) in order to contextualize the results for the quantum-gravity interface and to get a comparison with past experiments in various physical platforms. For this purpose, we first address the achievable gravitational force gradients  $|\nabla F|$ , then discuss the coherence lengths  $\xi$  achieved in this work.

For two gravitationally interacting objects, the masses and geometry of the involved objects set a limit on how large the force gradient can become. For compact objects (e.g., spheres) the limit is reached when the objects come close enough to touch. For large aspect ratio objects (e.g., membranes, cantilevers, beams), however, the force gradient typically saturates when the separation approaches the larger of the object's dimensions due to the distributed nature of the resulting gravitational interaction. The saturation behavior is studied in the Supplementary Text for representative cases, and the results are utilized for the comparisons below. Even if object sizes themselves allow for separations below 50  $\mu\text{m}$ , such separations currently have no meaning for gravity experiments due to complications that arise in shielding Casimir and other parasitic

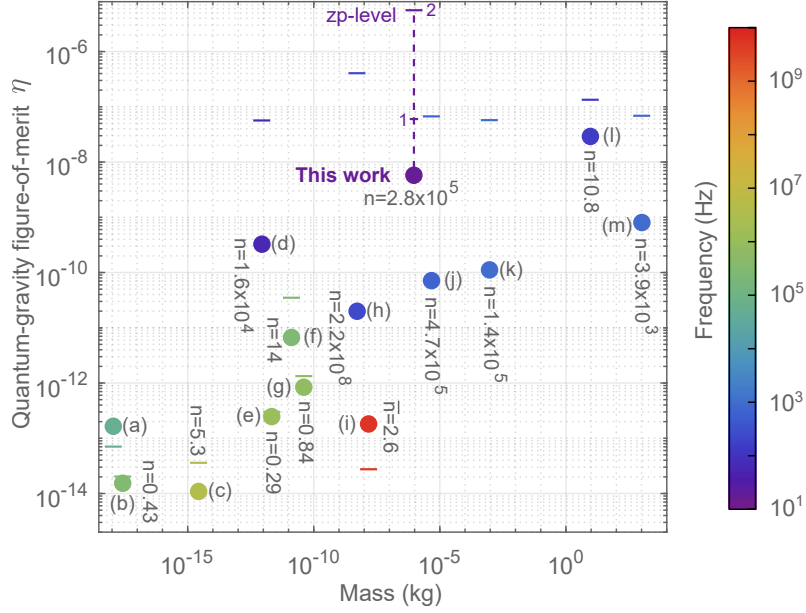


**Figure 3: Comparison to state-of-the-art mechanical quantum control experiments for utility at the quantum-gravity interface.** Colors encode oscillation mode frequencies.  $n$ : remaining mode excitation quanta after cooling. Data points come with their corresponding upper bar, indicating the hypothetical  $\eta$  level when the coherence length equals the zero-point (zp) fluctuations, i.e., when the oscillator is cooled to  $n = 0$ . Non-classical oscillator states (e.g. squeezed or Schrodinger cat states) can put the data points above their bars. Experiments: (a) nanosphere (42) — wavepacket expansion following  $n = 0.67$  cooling, (b) nanosphere (43), (c) nanobeam (44), (d) microsphere (45), (e) membrane (46), (f) cantilever (47), (g) membrane (48), (h) superconducting microsphere (12), (i) acoustic resonator (49) —  $\bar{n}$  indicating Schrodinger cat state size, (j) pendulum (36), (k) pendulum (35), (l) LIGO pendulums (41), (m) bar resonator (50). For ‘This work’, projected future performances are also indicated along the vertical dashed line; see main text.

electromagnetic interactions that would otherwise overshadow gravity. These shielding-related problems have been repeatedly encountered to date in gravity-related experiments, as well as in experiments with trapped ions in the form of electric field noise near conducting surfaces (51). For example, although gold screens with 100-nm-level thicknesses can easily be manufactured for electromagnetic shielding, parasitic interactions with screens due to patch potentials to date have prevented studying gravity below  $50 \mu\text{m}$  separations (52, 53).

To obtain coherence length values, we first calculate coherence angles, since we work with a torsional oscillator. Coherence angles can be found similarly to the coherence length of a linear oscillator, simply by replacing the linear zero-point fluctuations  $x_{zp}$  with its angular counterpart  $\theta_{zp} = \sqrt{\hbar/2I\omega_{\text{eff}}}$  —  $I$ : moment of inertia,  $\theta_{zp} = 1.2 \times 10^{-12}$  rad @  $\omega_{\text{eff}} = 2\pi \times 18$  Hz. Compared to a standard damping mechanism through a thermal bath, a careful analysis for the case of feedback damping reveals an additional suppression in the coherence angle (Supplementary Text):

$$\xi_{\theta} = s \theta_{zp} / \sqrt{2n + 1}. \quad (5)$$

Here,  $s = (1 + Q_{\text{eff}}^{-2} \Delta\theta_{\text{fb}}^2 / \Delta\theta^2)^{-1/2}$  is the suppression factor, which has noticeable effects only when the oscillator becomes near-critically damped, with the effect increasing for overdamping. The ratio  $\Delta\theta_{\text{fb}} / \Delta\theta$  is that of the feedback-imprinted-measurement-noise to the total-angular-noise, and can be extracted from the analysis in Figure 2B. For our range of parameters, this suppression makes at most a 20% deviation from the simple picture that omits  $s$ . The coherence angles evaluated for our experimental configurations are shown in the inset of Figure 2B. The implied coherence lengths  $\xi$  for the tip of the pendulum bar at  $d = 1$  mm from the rotation axis are also indicated. At the strongest damping, we obtain the largest coherence angle  $\xi_{\theta} = 1.2 \times 10^{-15}$  rad, resulting in the coherence length  $\xi = 1.2 \times 10^{-18}$  m — a thousandth of the size of an atomic nucleus.

Although  $\xi$  might appear small, at the crux of it all, it still enables the current system to distinguish itself in its utility for experiments at the quantum-gravity interface, leading to a figure-of-merit  $\eta = 0.6 \times 10^{-8}$ . To put this number into context, in Figure 3, we contrast it with the  $\eta$ -values that would have been achieved by other state-of-the-art mechanical quantum control experiments — we carefully lay out all the numbers and rationale that go into evaluating these figure-of-merit values in the Supplementary Text. Among physical systems that span more than 20 orders of magnitude in their masses, our intermediate-scale mass with its low frequency exhibits a distinct

performance while additionally offering a vast amount of improvement potential. This potential becomes particularly evident when contrasting to the readily achieved high performance of point (j) in the same figure — cooling of LIGO mirrors. While it utilizes technology very similar to ours, it requires at least 6 orders of magnitude more optical power than would be needed for our 1-mg pendulum to achieve ground-state cooling (54). To substantiate the improvement potential, note that in the current system we can realize a 65-mHz torsional oscillator by switching to a 1- $\mu\text{m}$ -diameter suspension fiber (e.g., (25)), and shifting the frequency to the 18 Hz value utilized in this work through feedback control will result in an apparent quality factor at the  $10^9$  scale. With the noise that exists in the current setup taken into account, a further 100-fold reduction in the effective temperatures can then be achieved (future projection level-1 in Fig. 3). Utilizing optical cavities engineered for torsional motion (54) will further allow cooling the system to its ground state (future projection level-2 in Fig. 3). Note that beyond ground-state cooling, utilization of squeezed states or wavepacket expansion techniques (as utilized in point (a) in Fig. 3) for the oscillators can dramatically increase the figure-of-merit in effect (29), which will allow pushing arbitrarily past projection level-2 (Fig. 3).

While its ability to offer a high  $\eta$  is a prerequisite for choosing a particular physical system, the domination of quantum noise — that is, the quantum coherence length approaching the total position uncertainty — is the necessity for the ability to generate gravitational entanglement. In our system, this regime is reached when the quantum radiation pressure noise (quantum backaction) is dominant over all other sources of noise — notably the thermal noise (17). While enabling ground-state cooling, this regime also enables entanglement protocols without the need for ground-state cooling (31, 32). Deterministic generation of entanglement between macroscopic objects has recently been demonstrated for the first time utilizing RF circuits as mediators between 10-micron-scale superconducting drum heads (55). Our demonstrated platform opens up an exciting path to carry over generation of such spooky correlations to gravitational systems and potentially unlock the biggest prize of all: cracking quantum gravity.

## Acknowledgments

We thank Johannes Fink and Scott Waitukaitis for their helpful feedback on the manuscript. This work was supported by Institute of Science and Technology Austria, and the European Research Council under Grant No. 101087907 (ERC CoG QuHAMP). O.H. conceived the experiment and supervised the project. M.M. manufactured the pendulum. S.A. and P.R. built the experimental setup. S.A. and O.H. performed the reported experiments, analyzed the data, and wrote the article.

## References

1. S. Bose, *et al.*, Massive quantum systems as interfaces of quantum mechanics and gravity (2023), <https://arxiv.org/abs/2311.09218>.
2. J. Oppenheim, A postquantum theory of classical gravity? *Physical Review X* **13** (4), 041040 (2023).
3. C. M. DeWitt, D. Rickles, The Role of Gravitation in Physics: Report from the 1957 Chapel Hill Conference. *Sources of Max Planck Research Library for the History and Development of Knowledge; Sources 5, Edition Open Access, Berlin* (2011).
4. S. Bose, *et al.*, Spin entanglement witness for quantum gravity. *Physical review letters* **119** (24), 240401 (2017).
5. C. Marletto, V. Vedral, Gravitationally induced entanglement between two massive particles is sufficient evidence of quantum effects in gravity. *Physical review letters* **119** (24), 240402 (2017).
6. M. Aspelmeyer, T. J. Kippenberg, F. Marquardt, Cavity optomechanics. *Rev. Mod. Phys.* **86**, 1391–1452 (2014), doi:10.1103/RevModPhys.86.1391, <https://link.aps.org/doi/10.1103/RevModPhys.86.1391>.
7. B. P. Abbott, *et al.*, Observation of Gravitational Waves from a Binary Black Hole Merger. *Phys. Rev. Lett.* **116**, 061102 (2016), doi:10.1103/PhysRevLett.116.061102, <https://link.aps.org/doi/10.1103/PhysRevLett.116.061102>.

8. T. Westphal, H. Hepach, J. Pfaff, M. Aspelmeyer, Measurement of gravitational coupling between millimetre-sized masses. *Nature* **591** (7849), 225–228 (2021), doi:10.1038/s41586-021-03250-7, <https://doi.org/10.1038/s41586-021-03250-7>.
9. T. M. Fuchs, *et al.*, Measuring gravity with milligram levitated masses. *Science Advances* **10** (8), eadk2949 (2024).
10. S. B. Cataño Lopez, J. G. Santiago-Condori, K. Edamatsu, N. Matsumoto, High- $Q$  Milligram-Scale Monolithic Pendulum for Quantum-Limited Gravity Measurements. *Phys. Rev. Lett.* **124**, 221102 (2020), doi:10.1103/PhysRevLett.124.221102, <https://link.aps.org/doi/10.1103/PhysRevLett.124.221102>.
11. N. Matsumoto, *et al.*, Demonstration of Displacement Sensing of a mg-Scale Pendulum for mm- and mg-Scale Gravity Measurements. *Phys. Rev. Lett.* **122**, 071101 (2019), doi:10.1103/PhysRevLett.122.071101, <https://link.aps.org/doi/10.1103/PhysRevLett.122.071101>.
12. J. Hofer, *et al.*, High- $Q$  Magnetic Levitation and Control of Superconducting Microspheres at Millikelvin Temperatures. *Phys. Rev. Lett.* **131**, 043603 (2023), doi:10.1103/PhysRevLett.131.043603, <https://link.aps.org/doi/10.1103/PhysRevLett.131.043603>.
13. T. Kawasaki, K. Komori, H. Fujimoto, Y. Michimura, M. Ando, Angular trapping of a linear-cavity mirror with an optical torsional spring. *Phys. Rev. A* **106**, 013514 (2022), doi:10.1103/PhysRevA.106.013514, <https://link.aps.org/doi/10.1103/PhysRevA.106.013514>.
14. K. Komori, *et al.*, Attonewton-meter torque sensing with a macroscopic optomechanical torsion pendulum. *Phys. Rev. A* **101**, 011802 (2020), doi:10.1103/PhysRevA.101.011802, <https://link.aps.org/doi/10.1103/PhysRevA.101.011802>.
15. N. K. Raut, J. Miller, J. Pate, R. Chiao, J. E. Sharping, Meissner Levitation of a Millimeter-Size Neodymium Magnet Within a Superconducting Radio Frequency Cavity. *IEEE Transactions on Applied Superconductivity* **31** (5), 1–4 (2021), doi:10.1109/TASC.2021.3053206.
16. K. Agatsuma, *et al.*, Precise measurement of laser power using an optomechanical system. *Optics express* **22** (2), 2013–2030 (2014).

17. Y. Michimura, K. Komori, Quantum sensing with milligram scale optomechanical systems. *The European Physical Journal D* **74** (6), 126 (2020), doi:10.1140/epjd/e2020-10185-5, <https://doi.org/10.1140/epjd/e2020-10185-5>.
18. M. Aspelmeyer, When zeh meets feynman: How to avoid the appearance of a classical world in gravity experiments (2022).
19. D. Vitali, *et al.*, Optomechanical Entanglement between a Movable Mirror and a Cavity Field. *Phys. Rev. Lett.* **98**, 030405 (2007), doi:10.1103/PhysRevLett.98.030405, <https://link.aps.org/doi/10.1103/PhysRevLett.98.030405>.
20. H. Müller-Ebhardt, H. Rehbein, R. Schnabel, K. Danzmann, Y. Chen, Entanglement of macroscopic test masses and the standard quantum limit in laser interferometry. *Physical review letters* **100** (1), 013601 (2008).
21. S. Bose, K. Jacobs, P. L. Knight, Scheme to probe the decoherence of a macroscopic object. *Phys. Rev. A* **59**, 3204–3210 (1999), doi:10.1103/PhysRevA.59.3204, <https://link.aps.org/doi/10.1103/PhysRevA.59.3204>.
22. W. Marshall, C. Simon, R. Penrose, D. Bouwmeester, Towards Quantum Superpositions of a Mirror. *Phys. Rev. Lett.* **91**, 130401 (2003), doi:10.1103/PhysRevLett.91.130401, <https://link.aps.org/doi/10.1103/PhysRevLett.91.130401>.
23. C. C. Gan, C. M. Savage, S. Z. Scully, Optomechanical tests of a Schrödinger-Newton equation for gravitational quantum mechanics. *Phys. Rev. D* **93**, 124049 (2016), doi:10.1103/PhysRevD.93.124049, <https://link.aps.org/doi/10.1103/PhysRevD.93.124049>.
24. L. Diósi, Testing Spontaneous Wave-Function Collapse Models on Classical Mechanical Oscillators. *Phys. Rev. Lett.* **114**, 050403 (2015), doi:10.1103/PhysRevLett.114.050403, <https://link.aps.org/doi/10.1103/PhysRevLett.114.050403>.
25. D. Carney, *et al.*, Mechanical quantum sensing in the search for dark matter. *Quantum Science and Technology* **6** (2), 024002 (2021), doi:10.1088/2058-9565/abcfcd, <https://dx.doi.org/10.1088/2058-9565/abcfcd>.

26. S. Qvarfort, D. Rätzel, S. Stopyra, Constraining modified gravity with quantum optomechanics. *New Journal of Physics* **24** (3), 033009 (2022).
27. C. Timberlake, A. Vinante, F. Shankar, A. Lapi, H. Ulbricht, Probing modified gravity with magnetically levitated resonators. *Physical Review D* **104** (10), L101101 (2021).
28. A. AlBalushi, W. Cong, R. B. Mann, Optomechanical quantum Cavendish experiment. *Physical Review A* **98** (4), 043811 (2018).
29. T. Krisnanda, G. Y. Tham, M. Paternostro, T. Paterek, Observable quantum entanglement due to gravity. *npj Quantum Information* **6** (1), 12 (2020), doi:10.1038/s41534-020-0243-y, <https://doi.org/10.1038/s41534-020-0243-y>.
30. T. Weiss, M. Roda-Llodes, E. Torrontegui, M. Aspelmeyer, O. Romero-Isart, Large quantum delocalization of a levitated nanoparticle using optimal control: Applications for force sensing and entangling via weak forces. *Physical Review Letters* **127** (2), 023601 (2021).
31. H. Miao, D. Martynov, H. Yang, A. Datta, Quantum correlations of light mediated by gravity. *Phys. Rev. A* **101**, 063804 (2020), doi:10.1103/PhysRevA.101.063804, <https://link.aps.org/doi/10.1103/PhysRevA.101.063804>.
32. D. Miki, A. Matsumura, K. Yamamoto, Feasible generation of gravity-induced entanglement by using optomechanical systems. *arXiv preprint arXiv:2406.04361* (2024).
33. O. Bengyat, A. Di Biagio, M. Aspelmeyer, M. Christodoulou, Gravity Mediated Entanglement between Oscillators as Quantum Superposition of Geometries. *arXiv preprint arXiv:2309.16312* (2023).
34. G. Huyet, S. Franke-Arnold, S. M. Barnett, Superposition states at finite temperature. *Physical Review A* **63** (4), 043812 (2001).
35. T. Corbitt, *et al.*, Optical Dilution and Feedback Cooling of a Gram-Scale Oscillator to 6.9 mK. *Phys. Rev. Lett.* **99**, 160801 (2007), doi:10.1103/PhysRevLett.99.160801, <https://link.aps.org/doi/10.1103/PhysRevLett.99.160801>.

36. N. Matsumoto, K. Komori, S. Ito, Y. Michimura, Y. Aso, Direct measurement of optical-trap-induced decoherence. *Phys. Rev. A* **94**, 033822 (2016), doi:10.1103/PhysRevA.94.033822, <https://link.aps.org/doi/10.1103/PhysRevA.94.033822>.
37. J. R. Pratt, *et al.*, Nanoscale Torsional Dissipation Dilution for Quantum Experiments and Precision Measurement. *Phys. Rev. X* **13**, 011018 (2023), doi:10.1103/PhysRevX.13.011018, <https://link.aps.org/doi/10.1103/PhysRevX.13.011018>.
38. A. M. Gretarsson, G. M. Harry, Dissipation of mechanical energy in fused silica fibers. *Review of scientific instruments* **70** (10), 4081–4087 (1999).
39. See supplementary materials.
40. K. Komori, D. Ďurovčiková, V. Sudhir, Quantum theory of feedback cooling of an anelastic macromechanical oscillator. *Phys. Rev. A* **105**, 043520 (2022), doi:10.1103/PhysRevA.105.043520, <https://link.aps.org/doi/10.1103/PhysRevA.105.043520>.
41. C. Whittle, *et al.*, Approaching the motional ground state of a 10-kg object. *Science* **372** (6548), 1333–1336 (2021), doi:10.1126/science.abh2634, <https://www.science.org/doi/abs/10.1126/science.abh2634>.
42. M. Rossi, *et al.*, Quantum Delocalization of a Levitated Nanoparticle. *arXiv preprint arXiv:2408.01264* (2024).
43. U. Delić, *et al.*, Cooling of a levitated nanoparticle to the motional quantum ground state. *Science* **367** (6480), 892–895 (2020), doi:10.1126/science.aba3993, <https://www.science.org/doi/abs/10.1126/science.aba3993>.
44. D. J. Wilson, *et al.*, Measurement-based control of a mechanical oscillator at its thermal decoherence rate. *Nature* **524** (7565), 325–329 (2015), doi:10.1038/nature14672, <https://doi.org/10.1038/nature14672>.
45. F. Monteiro, *et al.*, Force and acceleration sensing with optically levitated nanogram masses at microkelvin temperatures. *Physical Review A* **101** (5), 053835 (2020).

46. M. Rossi, D. Mason, J. Chen, Y. Tsaturyan, A. Schliesser, Measurement-based quantum control of mechanical motion. *Nature* **563** (7729), 53–58 (2018), doi:10.1038/s41586-018-0643-8, <https://doi.org/10.1038/s41586-018-0643-8>.
47. D. Zoepfl, *et al.*, Kerr Enhanced Backaction Cooling in Magnetomechanics. *Phys. Rev. Lett.* **130**, 033601 (2023), doi:10.1103/PhysRevLett.130.033601, <https://link.aps.org/doi/10.1103/PhysRevLett.130.033601>.
48. M. Underwood, *et al.*, Measurement of the motional sidebands of a nanogram-scale oscillator in the quantum regime. *Phys. Rev. A* **92**, 061801 (2015), doi:10.1103/PhysRevA.92.061801, <https://link.aps.org/doi/10.1103/PhysRevA.92.061801>.
49. M. Bild, *et al.*, Schrödinger cat states of a 16-microgram mechanical oscillator. *Science* **380** (6642), 274–278 (2023), doi:10.1126/science.adf7553, <https://doi.org/10.1126/science.adf7553>.
50. A. Vinante, *et al.*, Feedback Cooling of the Normal Modes of a Massive Electromechanical System to Submillikelvin Temperature. *Phys. Rev. Lett.* **101**, 033601 (2008), doi:10.1103/PhysRevLett.101.033601, <https://link.aps.org/doi/10.1103/PhysRevLett.101.033601>.
51. D. Hite, K. McKay, D. P. Pappas, Surface science motivated by heating of trapped ions from the quantum ground state. *New journal of physics* **23** (10), 103028 (2021).
52. J. Lee, E. Adelberger, T. Cook, S. Fleischer, B. Heckel, New test of the gravitational  $1/r^2$  law at separations down to 52  $\mu\text{m}$ . *Physical Review Letters* **124** (10), 101101 (2020).
53. C. P. Blakemore, *et al.*, Search for non-Newtonian interactions at micrometer scale with a levitated test mass. *Physical Review D* **104** (6), L061101 (2021).
54. S. Agafonova, U. Mishra, F. Diorico, O. Hosten, Zigzag optical cavity for sensing and controlling torsional motion. *Phys. Rev. Res.* **6**, 013141 (2024), doi:10.1103/PhysRevResearch.6.013141, <https://link.aps.org/doi/10.1103/PhysRevResearch.6.013141>.

55. S. Kotler, *et al.*, Direct observation of deterministic macroscopic entanglement. *Science* **372** (6542), 622–625 (2021).
56. S. Franke-Arnold, G. Huyet, S. M. Barnett, Measures of coherence for trapped matter waves. *Journal of Physics B: Atomic, Molecular and Optical Physics* **34** (5), 945 (2001).
57. G. Agarwal, Master equations in phase-space formulation of quantum optics. *Physical Review* **178** (5), 2025 (1969).
58. C. Savage, D. Walls, Damping of quantum coherence: the master-equation approach. *Physical Review A* **32** (4), 2316 (1985).
59. C. Savage, D. Walls, Quantum coherence and interference of damped free particles. *Physical Review A* **32** (6), 3487 (1985).
60. H. M. Wiseman, G. J. Milburn, *Quantum measurement and control* (Cambridge university press) (2009).
61. A. C. Doherty, K. Jacobs, Feedback control of quantum systems using continuous state estimation. *Physical Review A* **60** (4), 2700 (1999).
62. C. M. Caves, G. J. Milburn, Quantum-mechanical model for continuous position measurements. *Physical Review A* **36** (12), 5543 (1987).
63. H. M. Wiseman, Quantum theory of continuous feedback. *Physical Review A* **49** (3), 2133 (1994).
64. A. Hopkins, K. Jacobs, S. Habib, K. Schwab, Feedback cooling of a nanomechanical resonator. *Physical Review B* **68** (23), 235328 (2003).
65. A. Rouillard, *et al.*, Measurement-based Feedback Control of a Quantum System in a Harmonic Potential. *arXiv preprint arXiv:2212.12292* (2022).
66. O. Ciftja, Electrostatic interaction energy between two coaxial parallel uniformly charged disks. *Results in Physics* **15**, 102684 (2019).

67. O. Ciftja, G. Paredes, M. Griffin, Mathematical expressions for a system of two identical uniformly charged rods. *Physica Scripta* **89** (11), 115803 (2014).
68. T. R. Corbitt, *Quantum noise and radiation pressure effects in high power optical interferometers*, Ph.D. thesis, Massachusetts Institute of Technology (2008).

# Supplementary Materials

## Experimental Methods

A	Optimal tilt sensing with a split photodiode	S2
B	Push-beam power control	S3
C	Yaw-motion feedback control and its noise	S4
D	Taking under control other pendulum modes	S6
E	Torque sensitivity	S7

## Supplementary Text

1	Quantum coherence length	S8
1.1	Thermal harmonic oscillator	S8
2	Damped harmonic oscillator	S9
2.1	Damping via thermal bath	S9
2.2	Quantum feedback damping	S10
2.3	Experimental extraction of the coherence length	S13
3	Figure of merit $\eta$ for different systems	S14
3.1	Geometry factors for evaluating $ \nabla F $	S14
3.2	Parameters used for $\eta$ comparisons	S16

## Experimental Methods

### A Optimal tilt sensing with a split photodiode

Here, we derive the optimal sensitivity achievable for tilt sensing using a split photodiode, and introduce the tilt sensitivity parameter utilized in the main text.

After reflection of a Gaussian beam incident on a pendulum tilted by an angle  $\theta$ , the beam will acquire a  $2\theta$  tilt with respect to an untilted reference axis. A beam tilt by angle  $2\theta$  is equivalent to introducing a position-dependent phase shift  $2\theta k_0 x$  on the beam, where  $x$  is the coordinate perpendicular to the propagation axis and  $k_0 = 2\pi/\lambda$  is the wave number in terms of the wavelength  $\lambda$ . For small angles, the phase factor can be expressed as  $e^{i2\theta k_0 x} \approx 1 + i2\theta k_0 x$ , and the reflected beam profile can be described as a sum of zeroth-order and first-order Hermit-Gauss modes, as we will illustrate. In the following, we will make use of the normalized Hermite-Gauss mode functions

$$\begin{aligned}\phi_0(x, z) &= \frac{2^{1/4}}{(\pi w^2(z))^{1/4}} e^{-x^2/w^2(z)} e^{-ik_0 x^2/2R(z)} e^{i\varphi(z)} \\ \phi_1(x, z) &= \phi_0(x, z) \frac{2x}{w(z)} e^{i\varphi(z)}.\end{aligned}\tag{S1}$$

Here,  $z$  is the propagation distance along the reference axis, and  $w(z)$ ,  $R(z)$  and  $\varphi(z)$  are the propagation-distance-dependent spot size, wavefront curvature, and Gouy phase, respectively. The Gouy phase covers a range of  $\pi$  radians as  $z$  goes from  $-\infty$  to  $\infty$ .

We will take the pendulum to be located at  $z_p$ . Right after the pendulum, the incident beam represented by the wave  $\psi(x, z_p) = \phi_0(x, z_p)$  at the location of the pendulum will evolve into

$$\begin{aligned}\psi'(x, z_p) &= \phi_0(x, z_p) e^{ik_0 2\theta x} \\ &\approx \phi_0(x, z_p) + i e^{-i\varphi(z_p)} \theta k_0 w(z_p) \phi_1(x, z_p)\end{aligned}\tag{S2}$$

indicating that the tilt scatters a small amplitude into the first-order Hermit-Gauss mode which is proportional to the spot size  $w(z_p)$  at the location of the pendulum. To quantify the fundamental sensitivity to a tilt, first note that Eq. S2 is compatible with the physical propagating beam given by the wave

$$\begin{aligned}\Psi(x, z) &= \phi_0(x, z) + i e^{-i\varphi(z_p)} \theta k_0 w(z_p) \phi_1(x, z) \\ &= \phi_0(x, z) \left( 1 + i e^{i(\varphi(z) - \varphi(z_p))} x \frac{2\theta k_0 w(z_p)}{w(z)} \right),\end{aligned}\tag{S3}$$

since  $\Psi(x, z_p) = \psi'(x, z_p)$ . A split detector measures the shift in the position of a beam by differencing the integrated intensities (proportional to  $|\Psi(x, z)|^2$ ) in the two halves of the space.

A metrologically relevant sensitivity parameter  $\mathcal{S}$  is the change of the split detector signal as a function of tilt angle:

$$\begin{aligned}\mathcal{S}(z) &= \frac{d}{d\theta} \left| \int_{-\infty}^0 |\Psi(x, z)|^2 dx - \int_0^{\infty} |\Psi(x, z)|^2 dx \right| \\ &= \frac{\sqrt{32\pi}}{\lambda} w(z_p) |Re[ie^{i(\varphi(z)-\varphi(z_p))}]|\end{aligned}\tag{S4}$$

Here, terms proportional to  $\theta^2$  have been omitted in evaluating the integral as per the small-angle approximation. With these definitions,  $1/(\mathcal{S}\theta)^2$  has the interpretation of the total number of photons required to resolve  $\theta$ . Note also that  $\mathcal{S}$  is related to the mean displacement-to-spot size ratio as  $\mathcal{S}(z) = \sqrt{\frac{8}{\pi}} \frac{d}{d\theta} \frac{\langle x \rangle_z}{w(z)}$ , where  $\langle x \rangle_z$  is the  $z$ -dependent mean displacement.

Given the range of the Gouy phase function  $\varphi(z)$ , mathematically, there always exists a location  $z_{\text{opt}}$  where  $|ie^{i(\varphi(z)-\varphi(z_p))}| = 1$  that maximizes  $\mathcal{S}(z)$  to a value independent of the beam size at  $z_{\text{opt}}$ :

$$\mathcal{S}_{\text{max}} \equiv \mathcal{S}(z_{\text{opt}}) = \frac{\sqrt{32\pi}}{\lambda} w(z_p)\tag{S5}$$

This is the fundamental upper limit to our tilt sensitivity parameter. In the main text,  $w(z)$  and  $w(z_p)$  are replaced with  $w$  and  $w_p$ , respectively, and  $\langle x \rangle_z$  is replaced with  $\delta(\theta)$  for notational simplicity.

The maximization performed does not readily provide the spot size  $w(z_{\text{opt}})$  where  $\mathcal{S}$  is maximized. It could happen that the beam is very small at this point and falls into the gap of the split detector. Nevertheless, this can be remedied by additional beam shaping following the tilt, since a set of lenses can be utilized to independently adjust the Gouy phase shift and the beam size as illustrated in Figure 1E of the main text.

## B Push-beam power control

The push beam power reflecting from the pendulum is incident on a photodiode, and the measured power is stabilized by a 300-kHz-bandwidth analog feedback circuit. The electronically variable set-point of the stabilization determines the push power the pendulum sees. The set-point takes in a sum of three input signals: 1) a precision DC voltage for setting the default operating power, 2) a signal for arbitrary power modulation, and 3) a signal coming from the quadrant photodiode for engineering feedback-based equations of motion. The modulation input of this circuitry was utilized in obtaining the susceptibility curves in Fig. 2(a), where a white noise signal was input to generate a driving torque. In the absence of the second and third inputs, the push beam operates

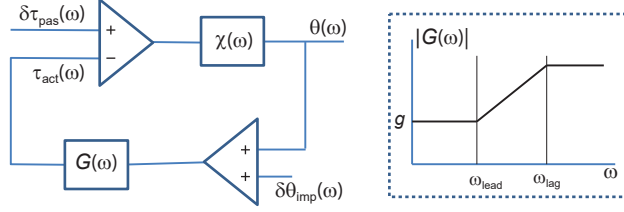


**Figure S1: Schematic of the feedback loop for yaw motion control.**

at a midpoint power of 2 mW with near-shot-noise-limited intensity fluctuations at all relevant frequencies.

### C Yaw-motion feedback control and its noise

Here, we explain the feedback circuit that controls the yaw motion, and derive the effective susceptibility as well as the feedback noise in the system.

The feedback loop is illustrated in Fig. S1. Expressed in the frequency domain, the controlled output of the system is the pendulum angle  $\theta(\omega)$ . This output is detected with an added angle equivalent imprecision noise  $\delta\theta_{\text{imp}}(\omega)$ , and fed into a loop filter with a transfer function  $G(\omega)$  determining how this signal is converted to an *active* feedback torque  $\tau_{\text{act}}(\omega)$  through the push beam. Additional *passive* torque noises  $\delta\tau_{\text{pas}}(\omega)$  also act on the system. The applied torques turn into a yaw angle through the natural mechanical susceptibility (torque-to-angle transfer function)  $\chi(\omega) = (\omega_0^2 - \omega^2 + i\omega\gamma(\omega))^{-1}/I$ , completing the loop. The passive torques consist of the thermal torque noise, the radiation pressure noise of the probe and push beams, and torques induced by vibration noise around the setup. In the current work, intensity fluctuations are near shot-noise limited, and the resulting total radiation pressure noise is at least three orders of magnitude smaller than thermal noise.

Self-consistency in the loop yields  $\theta = \chi(\delta\tau_{\text{pas}} - \tau_{\text{act}})$  with  $\tau_{\text{act}} = G(\theta + \delta\theta_{\text{imp}})$ . Solving for  $\theta$  gives

$$\theta(\omega) = \chi_{\text{eff}}(\omega)\delta\tau_{\text{pas}}(\omega) - \chi_{\text{imp}}(\omega)\delta\theta_{\text{imp}}(\omega), \quad (\text{S6})$$

where the effective susceptibility is  $\chi_{\text{eff}}(\omega) = \frac{\chi(\omega)}{1+G(\omega)\chi(\omega)}$ , and the imprecision noise transfer function is  $\chi_{\text{imp}}(\omega) = G(\omega)\chi_{\text{eff}}(\omega)$ . The dimensionless loop gain  $G(\omega)\chi(\omega)$  needs to satisfy the usual stability criterion ( $< 180^\circ$  phase shift at the unity loop gain) for the loop to be stable.

The loop transfer function is chosen as that of a variable-gain lead-lag compensation filter (Fig. S1)

$$G(\omega) = \frac{g}{\chi(0)} \frac{1 + i\omega/\omega_{\text{lead}}}{1 + i\omega/\omega_{\text{lag}}} \approx \frac{g}{\chi(0)} \left(1 + i\frac{\omega}{\omega_{\text{lead}}}\right). \quad (\text{S7})$$

Here,  $\omega_{\text{lead}}$  and  $\omega_{\text{lag}}$  are the start and stop frequencies of the linear gain increase, and the filter gain is chosen such that the DC loop gain  $G(0)\chi(0) = g$ . The approximation in Eq. S7 is valid for  $\omega_{\text{lead}} \ll \omega_{\text{lag}}$ . In our experiment,  $\omega_{\text{lag}} = 2\pi \times 1.5$  kHz and  $\omega_{\text{lead}} = \omega_{\text{eff}} Q_{\text{eff}} \left(1 - \frac{\omega_0^2}{\omega_{\text{eff}}^2}\right)$  has a minimum value of  $2\pi \times 7.7$  Hz for the case of  $\omega_{\text{eff}} = 2\pi \times 18$  Hz with critical damping  $Q_{\text{eff}} = 1/2$ , satisfying the approximation well. The unity gain point of the feedback loop needs to come before  $\omega_{\text{lag}}$  for loop stability, but the lag part of the filter is needed to make  $G(\omega)$  physical since no filter can have an endless gain increase with frequency. Utilizing the parameters in S7, the effective susceptibility  $\chi_{\text{eff}}(\omega)$  is given by

$$\begin{aligned} \chi_{\text{eff}}^{-1}(\omega) &= \chi^{-1}(\omega) + G(\omega) \\ &= I(\omega_{\text{eff}}^2 - \omega^2 + i\omega\gamma_{\text{eff}}) \end{aligned} \quad (\text{S8})$$

where  $\omega_{\text{eff}} = \omega_0 \sqrt{1 + g}$  and  $\gamma_{\text{eff}} = \frac{\omega_0^2 g}{\omega_{\text{lead}}} + \gamma(\omega)$ . Taking into account that  $\gamma_{\text{eff}} \gg \gamma(\omega)$  and  $\chi(0) = (I\omega_0^2)^{-1}$ , Eq. S7 can be rewritten as  $G(\omega) = I(\omega_{\text{eff}}^2) - \omega_0^2 + i\omega\gamma_{\text{eff}}$ , resulting into an explicit expression for the imprecision transfer function

$$\chi_{\text{imp}} = \frac{(\omega_{\text{eff}}^2) - \omega_0^2 + i\omega\gamma_{\text{eff}}}{(\omega_{\text{eff}}^2) - \omega^2 + i\omega\gamma_{\text{eff}}} \quad (\text{S9})$$

Note that all expressions that contain  $\gamma_{\text{eff}}$  can also be written in terms of  $Q_{\text{eff}} = \frac{\omega_{\text{eff}}}{\gamma_{\text{eff}}}$ , which is the primary quantity utilized for the experimental analysis in the main text.

Since all torque and measurement imprecision noises are mutually uncorrelated, the oscillator angular PSD can simply be expressed as

$$S_{\theta\theta}(\omega) = |\chi_{\text{eff}}(\omega)|^2 S_{\tau\tau}^{\text{pas}}(\omega) + |\chi_{\text{imp}}(\omega)|^2 S_{\theta\theta}^{\text{imp}}(\omega), \quad (\text{S10})$$

where the total passive torque PSD  $S_{\tau\tau}^{\text{pas}}$  is dominated by the suspension thermal noise with a small contribution from vibrations:  $S_{\tau\tau}^{\text{pas}}(\omega) \approx S_{\tau\tau}^{\text{th}}(\omega) + S_{\tau\tau}^{\text{vib}}(\omega)$ .

In comparison to a simple change in susceptibility, Eq. S10 shows that the feedback control additionally imprints some detection noise on the oscillation angle PSD. This becomes relatively more important only when the feedback loop tries to control the oscillation amplitude at the

measurement noise limit. Eq. S10 forms the basis of the spectral motion analysis under active control in the main text.

#### **D Taking under control other pendulum modes**

Robust manipulation of the yaw motion requires first taking many other modes of the pendulum under control. In our case, the primary reason for this surfaced when we needed to float the optical table hosting the experiment to reduce ground vibration noise above 5 Hz, such that thermal-noise-limited operation could be achieved. However, floating the table rendered the system unworkable due to the large swing-mode motions it induced. Another limitation was the yaw-motion feedback leading to instabilities in the higher-frequency violin modes of the pendulum.

To circumvent these problems, we mounted the vacuum chamber on the optical table from a single side, forming a cantilever-like structure with natural resonance around 65 Hz. We then actuated (pushed on) the chamber from two orthogonal directions with piezo transducers, gaining the capability of jiggling the pendulum suspension point in space. This led to a configuration where all modes other than the yaw mode were strongly affected by the piezos. The yaw motion was near-purely actuated by the push beam — due to the natural decoupling of torsional motion from suspension point motion. Note that the optical lever system and the QPD were mounted on the rigid optical table, measuring the true motion of the pendulum relative to the massive optical table.

Various levels of information were available on the QPD output for each of the pendulum modes, e.g., longitudinal and horizontal swings at 2.27 Hz, roll at 44.48 Hz, pitch at 125.95 Hz, 1<sup>st</sup> longitudinal and transverse violins at 74.40 Hz and 82.28 Hz, and 2<sup>nd</sup> longitudinal and transverse violins at 169.59 Hz and 178.80 Hz, etc. Note that for an ideal pendulum, no information is expected on the optical lever about the modes that give rise to motion in the transverse direction. However, a 2-degree tilt (from vertical) of the pendulum surface that resulted from a non-ideal gluing of the suspension fiber resulted in all transverse modes imprinting some information on the optical lever.

Each spectral line in the QPD signal was appropriately phase-shifted and amplified with analog electronics and fed back to the relevant piezo transducer to sufficiently dampen the corresponding mechanical mode. Additional details about this far-from-optimal feedback loop are beyond the scope of this article; however, the discussed challenges are not a show stopper for scaling the current setup to more sensitive versions. They just indicate that the vibration isolation architecture

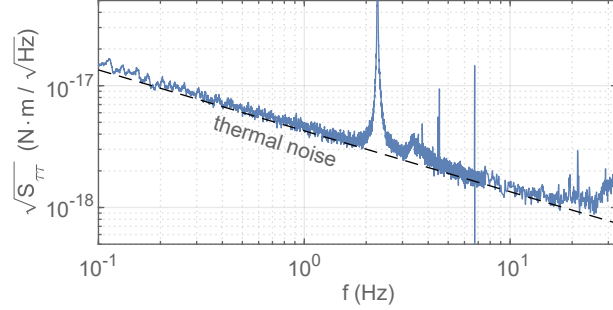


**Figure S2: Torque sensitivity.** Free running torque-referred angular noise  $S_{\tau\tau} \equiv S_{\theta\theta}/|\chi|^2$ , characterizing the torque sensitivity. The loss of sensitivity around 2.2 Hz is due to leakage of the pendulum swing mode signals into the yaw channel.

needs to be planned in advance to alleviate limitations due to ambient vibrations.

## E Torque sensitivity

In addition to the demonstrated optomechanical control capabilities, the developed pendulum system is very competitive as a sensor. The torque sensitivity is primarily limited by structural thermal noise, and reaches a minimal observed value of  $1.2 \times 10^{-18}$  around 20 Hz (Fig. S2). This corresponds to a broadband angular acceleration sensitivity of  $3.3 \times 10^{-6} \text{ rad} \cdot \text{s}^{-2}/\sqrt{\text{Hz}}$ , or, when referred to the tip of the pendulum, to a broadband linear acceleration sensitivity of  $3.3 \times 10^{-10} \text{ g}/\sqrt{\text{Hz}}$ . This value is on par with state-of-the-art *resonant* acceleration sensitivities achievable with magnetically levitated particles at the 1-milligram level in cryogenic systems (9).

While achieving a factor of 10 beyond state-of-the-art torque sensitivity at the milligram scale (14), this thermal-noise-limited sensitivity allows for a very clear demonstration of the peculiar properties of structural damping for nearly three decades of a frequency range in our setup —  $1/f$  noise in  $S_{\tau\tau}(f)$  instead of white noise.

## Supplementary Text

### 1 Quantum coherence length

Following pioneering interference experiments with trapped ions, the concept of a coherence length for matter waves was rigorously developed in references (34, 56), in analogy to optical coherence. The main outcome that is useful for our purposes is the definition of the coherence length  $\xi$ :

$$\xi^2 = \frac{\text{Tr}(\hat{\rho}^2 \hat{x}^2) - \text{Tr}(\hat{\rho} \hat{x} \hat{\rho} \hat{x})}{\text{Tr}(\hat{\rho}^2)}. \quad (\text{S11})$$

Here,  $\hat{\rho}$  is the quantum-mechanical density operator and  $\hat{x}$  is the position operator of the object. In terms of the density matrix elements  $\rho(x, x') = \langle x | \hat{\rho} | x' \rangle$ , the above expression can be written as

$$\xi^2 = \frac{\int_{-\infty}^{\infty} \int_{-\infty}^{\infty} dx dx' |\rho(x, x')|^2 \frac{1}{2} (x - x')^2}{\int_{-\infty}^{\infty} \int_{-\infty}^{\infty} dx dx' |\rho(x, x')|^2} \quad (\text{S12})$$

Changing variables to  $x \rightarrow x + \frac{\Delta}{2}$  and  $x' \rightarrow x - \frac{\Delta}{2}$  to make the dependence on the off-diagonal ( $x \neq x'$ ) elements explicit, and defining the shorthand notation  $|g(\Delta)|^2 = \int_{-\infty}^{\infty} dx |\rho(x + \frac{\Delta}{2}, x - \frac{\Delta}{2})|^2$ , we reach a compact form of the coherence length equation

$$\xi^2 = \frac{1}{2} \frac{\int_{-\infty}^{\infty} d\Delta |g(\Delta)|^2 \Delta^2}{\int_{-\infty}^{\infty} d\Delta |g(\Delta)|^2}. \quad (\text{S13})$$

Here,  $|g(\Delta)|^2$  is a position-averaged version of the off-diagonal elements of the density matrix. Equation S13 extracts the mean range of the off-diagonal density matrix elements, forming a direct relationship to fringe visibility in matter wave interference experiments.

#### 1.1 Thermal harmonic oscillator

In the Sudharsan P representation, a thermal state of a harmonic oscillator can be expressed as an incoherent mixture of coherent states  $|\alpha\rangle$  with  $\alpha = \alpha_{\text{re}} + i\alpha_{\text{im}}$  the complex amplitude:

$$\hat{\rho} = \int d^2\alpha \frac{1}{\pi n_0} e^{-|\alpha|^2/n_0} |\alpha\rangle \langle \alpha|. \quad (\text{S14})$$

Here  $n_0$  is the mean thermal excitation quanta, and the integration is over the whole complex plane. Given the projection onto the position basis elements  $\langle x | \alpha \rangle = \left(\frac{1}{2\pi x_{zp}^2}\right)^{1/4} \exp\left[-\frac{(x - 2x_{zp}\alpha_{\text{re}})^2}{4x_{zp}^2} + \right.$

$i\frac{\alpha_{\text{im}}x}{x_{zp}} - i\alpha_{\text{im}}\alpha_{\text{re}}]$ , where  $x_{zp}^2$  is the ground state position variance, the density matrix elements can be expressed as

$$\rho(x + \frac{\Delta}{2}, x - \frac{\Delta}{2}) = \sqrt{\frac{1}{2\pi\sigma_x^2}} e^{-x^2/2\sigma_x^2} e^{-\Delta^2/2\sigma_\Delta^2}, \quad (\text{S15})$$

where  $\sigma_x^2 = x_{zp}^2(2n_0 + 1)$  and  $\sigma_\Delta^2 = 4x_{zp}^2/(2n_0 + 1)$ . Thus, for the coherence length  $\xi$  and the position uncertainty  $\Delta x \equiv \text{Tr}[\hat{\rho}\hat{x}^2]^{1/2}$ , we obtain

$$\begin{aligned} \xi &= \frac{1}{2}\sigma_\Delta = x_{zp}/\sqrt{2n_0 + 1}, \\ \Delta x &= \sigma_x = x_{zp}\sqrt{2n_0 + 1}. \end{aligned} \quad (\text{S16})$$

These expressions indicate that the coherence length shrinks with increasing temperature in contrast to a growing overall position uncertainty — with the product  $\xi \cdot \Delta x = x_{zp}^2$  constant.

## 2 Damped harmonic oscillator

In this section, we will describe the behavior of a damped harmonic oscillator from an open quantum systems point of view, using master equations. We will see how the system equilibrates in a thermal quantum state. We will look into both the case of damping due to coupling to a high-temperature bath and the more complicated case of active feedback damping. For the latter case, we will see deviations from the ideal thermal state result near the oscillator's ground state, as well as when the system approaches the overdamped region. Our main focus will be on extracting coherence lengths.

### 2.1 Damping via thermal bath

A master equation for a harmonic oscillator coupled to a thermal bath was derived in reference (57) in the Markov and Born approximations and further studied in the density matrix formalism, for example, in references (58–60) to understand quantum coherence and interference phenomena in damped systems. The density matrix master equation reads

$$\frac{d}{dt}\hat{\rho} = \frac{1}{i\hbar}[\hat{H}_0, \hat{\rho}] + \frac{1}{i\hbar}\frac{\gamma_0}{2}[\hat{x}, \hat{p}\hat{\rho} + \hat{\rho}\hat{p}] - \frac{D_{th}}{\hbar^2}[\hat{x}, [\hat{x}, \hat{\rho}]]. \quad (\text{S17})$$

The first term in the rate of change of the density operator describes the unitary part of the evolution with the free Hamiltonian for an oscillator of angular frequency  $\Omega$  given by  $\hat{H}_0 = \frac{1}{2m}\hat{p}^2 + \frac{1}{2}m\Omega^2\hat{x}^2$ . The second term describes the damping with the energy decay rate  $\gamma_0$ . The last term describes the noise introduced due to the coupling to the thermal bath, and gives rise to a diffusion in momentum

with a diffusion constant  $D_{th} = \gamma_0 \hbar^2 (2n_0 + 1) / 4x_{zp}^2 \approx \gamma_0 m k_B T$ . This term at the same time gives rise to an associated decoherence in position basis. The fact that Eq. S17 gives rise to velocity damping can be seen through evaluation of the expectation values of the position and momentum operators. The expectation value  $\langle \hat{O} \rangle \equiv Tr(\hat{\rho} \hat{O})$  for an arbitrary operator  $\hat{O}$  under the evolution equation Eq. S17 is given by  $\frac{d}{dt} \langle \hat{O} \rangle = \frac{1}{i\hbar} \langle [\hat{O}, \hat{H}_0] \rangle + \frac{1}{i\hbar} \frac{\gamma_0}{2} \langle \{ [\hat{O}, \hat{x}], \hat{p} \} \rangle - \frac{D_{th}}{\hbar^2} \langle [[\hat{O}, \hat{x}], \hat{x}] \rangle$  — the curly brackets represent the anti-commutator. Then, one obtains the equations of motion for the first moments

$$\begin{aligned} \frac{d}{dt} \langle \hat{x} \rangle &= \frac{1}{m} \langle \hat{p} \rangle \\ \frac{d}{dt} \langle \hat{p} \rangle &= -m\Omega^2 \langle \hat{x} \rangle - \gamma_0 \langle \hat{p} \rangle, \end{aligned} \quad (\text{S18})$$

yielding the dynamical equations for a damped harmonic oscillator  $(\frac{d^2}{dt^2} + \gamma_0 \frac{d}{dt} + \Omega^2) \langle \hat{x} \rangle = 0$ . It can also be seen that the diffusion term enters the equations of motion for the second moment of the momentum:  $\frac{d}{dt} \langle \hat{p}^2 \rangle \supset 2D_{th}$ .

Projecting Eq. S17 onto position basis and utilizing  $\hat{p} = -i\hbar \int dx |x\rangle \frac{\partial}{\partial x} \langle x|$ , one obtains the evolution equation for the density matrix elements in position basis:

$$\begin{aligned} \frac{d}{dt} \rho(x, x') &= \left[ \frac{1}{i\hbar} \left( \frac{-\hbar^2}{2m} \left( \frac{\partial^2}{\partial x^2} - \frac{\partial^2}{\partial x'^2} \right) + \frac{m\Omega^2}{2} (x^2 - x'^2) \right) \right. \\ &\quad \left. - \frac{\gamma_0}{2} (x - x') \left( \frac{\partial}{\partial x} - \frac{\partial}{\partial x'} \right) - \frac{D_{th}}{\hbar^2} (x - x')^2 \right] \rho(x, x'). \end{aligned} \quad (\text{S19})$$

In the variables that make the off-diagonal elements explicit, i.e.,  $\rho \equiv \rho(x + \frac{\Delta}{2}, x - \frac{\Delta}{2})$ ,

$$\frac{d}{dt} \rho = \left[ \frac{1}{i\hbar} \left( \frac{-\hbar^2}{m} \frac{\partial^2}{\partial x \partial \Delta} + m\Omega^2 x \Delta \right) - \gamma_0 \Delta \frac{\partial}{\partial \Delta} - \frac{D_{th}}{\hbar^2} \Delta^2 \right] \rho. \quad (\text{S20})$$

The solution to this equation in steady state (obtained by setting  $\frac{d}{dt} \rho = 0$ ) is of the same form as Eq. S15. The solution is a thermal state with coherence length and position uncertainty given again by Eq. S16.

## 2.2 Quantum feedback damping

Before writing down a master equation for the case of feedback-based damping, we will first address a subtlety associated with the description of the implementation of a velocity feedback force. This arises because of the lack of clarity on how to incorporate the time derivative of position into a Hamiltonian description.

We are interested in implementing a feedback force  $F_{\text{fb}}(t) = -m\gamma_{\text{eff}}\frac{d}{dt}x_{\text{obs}}(t)$ , containing the time derivative of the continuously observed position  $x_{\text{obs}}(t)$  to achieve a velocity damping force with an effective energy damping rate  $\gamma_{\text{eff}}$ . Thus we would like to implement the Hamiltonian

$$\begin{aligned}\hat{H} &= \hat{H}_0 + \hat{H}_{\text{fb}} \\ \hat{H}_0 &= \frac{1}{2m}\hat{p}^2 + \frac{1}{2}m\Omega^2x^2 \\ \hat{H}_{\text{fb}} &= -\hat{x}F_{\text{fb}} = \hat{x}m\gamma_{\text{eff}}\frac{dx_{\text{obs}}}{dt}\end{aligned}\quad (\text{S21})$$

To simplify the description, we first go to an equivalent Hamiltonian formulation of the same physical situation utilizing the unitary transformation  $\hat{T} = \exp[i\zeta(\hat{x}, t)/\hbar]$ . Now, the states in the new description (primed) are related to the old description by  $|\psi'\rangle = \hat{T}|\psi\rangle$ , or more generally, the relation to the old density matrix is  $\hat{\rho}' = \hat{T}\hat{\rho}\hat{T}^\dagger$ . The new Hamiltonian is related to the old one by  $\hat{H}' = \hat{T}\hat{H}\hat{T}^\dagger - \frac{\partial\zeta}{\partial t}$ , where the nontrivial part of the transformation arises from  $\hat{T}\hat{p}\hat{T}^\dagger = \hat{p} - \frac{\partial\zeta}{\partial x}$ . A judicious choice of  $\zeta(\hat{x}, t)$  transforms the problem into what is called a *direct feedback* (61) as opposed to an estimation-based feedback. Choosing  $\zeta(\hat{x}, t) = \hat{x}m\gamma_{\text{eff}}x_{\text{obs}}(t)$ , we obtain

$$\hat{H}' = \hat{H}_0 - x_{\text{obs}}(t)\gamma_{\text{eff}}\hat{p}\quad (\text{S22})$$

up to an additional operator independent term. The physical observables change form in the new description. While  $[\hat{x}, \hat{p}] = i\hbar$  still holds and the role of the position operator remains the same in the new representation, the operator  $\hat{p}_{\text{kin}} = \hat{p} - m\gamma_{\text{eff}}x_{\text{obs}}(t)$  becomes the new kinematical momentum that physically corresponds to the observable  $\hat{p}$  in the first description. For example, the physical operator corresponding to the kinetic energy is now  $\frac{1}{2m}\hat{p}_{\text{kin}}^2$ . The magnitude of the density matrix elements  $|\rho(x, x')|$ , which is the quantity of interest, remains unchanged between the two representations, since the transformation is only a position-dependent phase shift.

Measurement and feedback based on the Hamiltonian in Eq. S22 is well studied (60, 62–65). Ignoring the negligible intrinsic damping  $\gamma_0$  with respect to the much larger feedback damping rate  $\gamma_{\text{eff}}$  — but keeping the thermal noise due to the intrinsic damping — the unconditional master equation for the density matrix for the current problem can be expressed as

$$\frac{d}{dt}\hat{\rho} = \frac{1}{i\hbar}[H_0, \hat{\rho}] - \frac{1}{i\hbar}\frac{\gamma_{\text{eff}}}{2}[\hat{p}, \hat{x}\hat{\rho} + \hat{\rho}\hat{x}] - \left(\frac{D_{th}}{\hbar^2} + \frac{D_m}{\hbar^2}\right)[\hat{x}, [\hat{x}, \hat{\rho}]] - \frac{D_{\text{fb}}}{\hbar^2}[\hat{p}, [\hat{p}, \hat{\rho}]]\quad (\text{S23})$$

Unlike the case in Eq. S18, the equations of motion for the expectation values of position and

momentum read

$$\begin{aligned}\frac{d}{dt}\langle\hat{x}\rangle &= \frac{1}{m}\langle\hat{p}\rangle - \gamma_{\text{eff}}\langle\hat{x}\rangle, \\ \frac{d}{dt}\langle\hat{p}\rangle &= -m\Omega^2\langle\hat{x}\rangle,\end{aligned}\tag{S24}$$

but, still yield the same dynamical equations for the damped harmonic oscillator ( $\frac{d^2}{dt^2} + \gamma_{\text{eff}}\frac{d}{dt} + \Omega^2$ ) $\langle\hat{x}\rangle = 0$ . In Eq. S23, the second term is responsible for the damping caused by the feedback. The third term now contains an additional diffusion constant  $D_m$  that leads to extra momentum diffusion due to the measurement backaction. For our purposes,  $D_m$  phenomenologically quantifies the measurement strength as well as the associated positional decoherence strength. The last term leads to a new position diffusion (diffusion constant  $D_{\text{fb}}$ ) due to feeding back a noisy signal to the system — showing up in the equation of motion for the second moment of the position:  $\frac{d}{dt}\langle\hat{x}^2\rangle \supset 2D_{\text{fb}}$ . For unit detection efficiency, one would have  $D_{\text{fb}} = \hbar^2\gamma_{\text{eff}}^2/16D_m$ . The master equation for the density matrix elements  $\rho \equiv \rho(x + \frac{\Delta}{2}, x - \frac{\Delta}{2})$  now takes the form

$$\frac{d}{dt}\rho = \left[ \frac{1}{i\hbar} \left( \frac{-\hbar^2}{m} \frac{\partial^2}{\partial x \partial \Delta} + m\Omega^2 x \Delta \right) - \gamma_{\text{eff}} \left( 1 + x \frac{\partial}{\partial x} \right) - \left( \frac{D_{th}}{\hbar^2} + \frac{D_m}{\hbar^2} \right) \Delta^2 + D_{\text{fb}} \frac{\partial^2}{\partial x^2} \right] \rho. \tag{S25}$$

The solution to this equation in steady state is

$$\rho(x + \frac{\Delta}{2}, x - \frac{\Delta}{2}) = \sqrt{\frac{1}{2\pi\sigma_x^2}} e^{-x^2/2\sigma_x^2} e^{-\Delta^2/2\sigma_\Delta^2} e^{ibx\Delta}. \tag{S26}$$

In the limit in which measurement backaction (radiation pressure noise) is negligible with respect to the thermal noise ( $D_m \ll D_{th}$ ) and in which the imprinted feedback noise is subdominant to thermal noise ( $4D_{th}x_{zp}^2/\hbar^2 > D_{\text{fb}}/x_{zp}^2$ ) — as are the cases for our experiment — position uncertainty  $\Delta x \equiv \sigma_x$  and coherence length  $\xi = \frac{1}{2}\sigma_\Delta$  read

$$\begin{aligned}\Delta x &= x_{zp} \left( \frac{\gamma_0}{\gamma_{\text{eff}}} (2n_0 + 1) + \frac{\Delta x_{\text{fb}}^2}{x_{zp}^2} \right)^{1/2} \equiv x_{zp} \sqrt{2n + 1}, \\ \xi &= x_{zp} \left( \frac{\gamma_0}{\gamma_{\text{eff}}} (2n_0 + 1) + \frac{\Delta x_{\text{fb}}^2}{x_{zp}^2} (1 + Q_{\text{eff}}^{-2}) \right)^{-1/2}.\end{aligned}\tag{S27}$$

Here, the quality factor is defined as  $Q_{\text{eff}} = \Omega/\gamma_{\text{eff}}$ , and the measurement noise imprinted by the feedback as  $\Delta x_{\text{fb}} = (D_{\text{fb}}/\gamma_{\text{eff}})^{1/2}$ . The definition for calculating the effective mean thermal excitation quanta  $n$  is also indicated. We see that the feedback itself acts to reduce the initial excitation numbers by a factor of  $\frac{\gamma_0}{\gamma_{\text{eff}}}$ . On the other hand, looking at the first of Eqs. S27, we see that the imprinted measurement noise  $\Delta x_{\text{fb}}$  due to the feedback tends to do the opposite action — but it

is subdominant in our range of parameters. The second of Eqs. S27 shows that the negative effect of the imprinted measurement noise starts to get amplified from the perspective of the coherence length as one approaches critical damping. Depending on the magnitude of the feedback noise, this amplified contribution could thus become important in our range of parameters. Eq. S27 is to be contrasted with the thermal bath damping results, Eq. S16, where the excess terms due to feedback are absent.

### 2.3 Experimental extraction of the coherence length

First, note that the utilized master equation description assumes an infinite feedback bandwidth. Given that our pendulum operates at 18 Hz, and our feedback loop maintains the velocity damping character up to 1.5 kHz, the infinite bandwidth assumption holds well, as the susceptibility of our torsional oscillator rapidly declines above resonance. In addition, note that excess detection noise or excess vibration noise can be bundled into the phenomenological momentum and position diffusion coefficients  $D_{th}$  and  $D_{fb}$  without the need for a change in the model.

To translate the results of the linear harmonic oscillator into those of a torsional oscillator, we simply need to replace the linear zero-point fluctuation level  $x_{zp}$  with its angular counterpart  $\theta_{zp} = \sqrt{\hbar/2I\Omega}$ , where  $I$  is the moment of inertia. Then, we obtain the angular analogues of Eqs. S27:

$$\begin{aligned}\Delta\theta &= \theta_{zp} \left( \frac{\gamma_0}{\gamma_{\text{eff}}} (2n_0 + 1) + \frac{\Delta\theta_{\text{fb}}^2}{\theta_{zp}^2} \right)^{1/2} \equiv \theta_{zp} \sqrt{2n + 1}, \\ \xi_\theta &= \theta_{zp} \left( \frac{\gamma_0}{\gamma_{\text{eff}}} (2n_0 + 1) + \frac{\Delta\theta_{\text{fb}}^2}{\theta_{zp}^2} (1 + Q_{\text{eff}}^{-2}) \right)^{-1/2}.\end{aligned}\tag{S28}$$

For experimental analysis, these two equations can be combined to yield a simpler coherence angle expression

$$\xi_\theta = s \theta_{zp} / \sqrt{2n + 1}\tag{S29}$$

in terms of the effective mean excitation quanta  $n$  and an additional suppression factor  $s = (1 + Q_{\text{eff}}^{-2} \Delta\theta_{\text{fb}}^2 / \Delta\theta^2)^{-1/2}$ . This suppression factor has an effect only when the oscillator becomes near-critically damped, with the effect increasing for overdamping. The variance ratio  $\Delta\theta_{\text{fb}}^2 / \Delta\theta^2$  is experimentally available through the imprinted noise modeling in the context of Fig. 2B that utilizes Eq. S10. Following the method discussed in the main text for extracting ratios of variances

through their PSDs (Eq. 4), this ratio can be evaluated as

$$\frac{\Delta\theta_{\text{fb}}^2}{\Delta\theta^2} = \frac{\int_{f_1}^{f_2} |\chi_{\text{imp}}(f)|^2 S_{\theta\theta}^{\text{imp}}(f) df}{\int_{f_1}^{f_2} S_{\theta\theta}(f) df}, \quad (\text{S30})$$

again with  $f_1 = 8$  Hz and  $f_2 = 28$  Hz. Recall that  $\chi_{\text{imp}}(f)$  is the transfer function in Eq. S9 for the experimentally characterized measurement imprecision noise  $S_{\theta\theta}^{\text{imp}}(f)$ .

Eq. S29 is what we use to extract coherence angles  $\xi_\theta$  in the main text. The conversion of this angular coherence to a linear coherence length  $\xi$  for the tip of the pendulum bar is accomplished by multiplying by half the length of the pendulum bar.

### 3 Figure of merit $\eta$ for different systems

Detailed comparisons of systems with vastly differing properties for their utility at the quantum-gravity interface can be tedious. Especially, when the aspect ratios of the objects become large, a calculation is needed to assess the distributed nature of the interaction for proper comparison. Nevertheless, it is still possible to draw general conclusions by classifying objects into a few basic geometrical categories. A further complication arises when considering the oscillation-mode structures, e.g., higher-order standing-wave modes in a membrane, or standing-wave modes in a cantilever. In order to prevent underestimations of  $\eta$  values, we make a gravitationally-overestimating assumption, and pretend that the entire object moves uniformly with the amplitude of the relevant mode, dispensing of mode structures for ease of comparison.

#### 3.1 Geometry factors for evaluating $|\nabla F|$

The quantity of interest that enters  $\eta$  is the force gradient between the two objects with respect to their separation  $d$ . Given two extended objects and their gravitational interaction energy  $U[d]$  that appears in the system Hamiltonian, the force gradient between the objects is the second derivative of the interaction energy:  $|\nabla F| = |\partial^2 U / \partial d^2|$ . Taking two identical objects with uniform mass densities and equal masses  $m$ , we will calculate the force gradients for three umbrella cases to cover all types of objects. The 3D calculation is intended to cover spherical, and other small aspect ratio objects; the 2D calculation is intended to cover membrane-like objects; and the 1D calculation is intended to cover objects like beams, rods, and cantilevers. Comparing the geometry functions obtained in each

case will show us how the associated force gradients saturate as the object separation approaches the major physical dimensions of each type of object.

**3D** – Two spherical point particles of mass  $m$  each, separated by  $d$ .

The gravitational interaction energy of two point particles can be written as  $U[d] = -\frac{Gm^2}{d}$ . The resulting force gradient is  $|\nabla F| = 2\frac{Gm^2}{d^3} = 2\frac{Gm^2}{L^3}f_{3D}[d/L]$ . The factor

$$f_{3D}[a] = 1/a^3 \quad (\text{S31})$$

encodes the geometry of the problem, and is introduced through the arbitrary length scale  $L$  to compare with the other cases, where real length scales do exist.

**2D** – Two parallel thin disks with diameter  $L$  and mass  $m$  each, separated axially by  $d$ .

The problem of charged interacting disks in electrostatics has been well studied (66). Borrowing from the results of these works, the analogous gravitational interaction energy of two disks can be written as  $U[d, R] = -\frac{Gm^2}{L}g_{2D}[d/L]$ , where the function  $g_{2D}$  encoding the geometry of the problem is given in terms of the Bessel function  $J_1[u]$  of the first kind as  $g_{2D}[a] = 8\int_0^\infty du \left(\frac{J_1[u]}{u}\right)^2 e^{-2au}$ . The resulting force gradient is  $|\nabla F| = 2\frac{Gm^2}{L^3}f_{2D}[d/L]$ , where the geometry factor is

$$f_{2D}[a] = 16\int_0^\infty du J_1[u]^2 e^{-2au}. \quad (\text{S32})$$

**1D** – Two parallel thin rods with length  $L$  and mass  $m$  each, separated by  $d$ .

The problem of charged interacting rods in electrostatics has been well studied (67). Borrowing from the results of these works, the analogous gravitational interaction energy of two rods can be written as  $U[d, L] = -\frac{Gm^2}{L}g_{1D}[d/L]$ , where the function  $g_{1D}[a] = \ln\left[\frac{1+\sqrt{1+a^2}}{-1+\sqrt{1+a^2}}\right] - 2\sqrt{1+a^2} + 2a$  encodes the geometry of the problem. The resulting force gradient is  $|\nabla F| = 2\frac{Gm^2}{L^3}f_{1D}[d/L]$ , where the geometry factor is

$$f_{1D}[a] = \frac{1}{a^2\sqrt{1+a^2}}. \quad (\text{S33})$$

Given that the prefactors of  $|\nabla F|$  have been arranged in the same form with respect to the reference length in all cases, to study the saturation behavior of the force gradient, we simply need

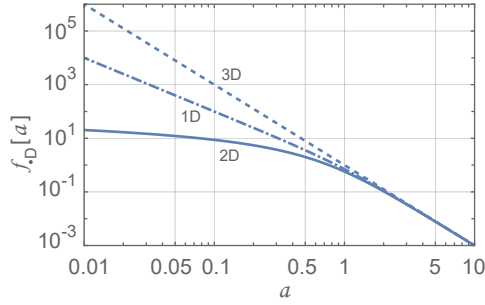


**Figure S3: Comparison of the geometry factors  $f_{\text{D}}[a]$  that describe the force gradient  $|\nabla F|$  for different object geometries.** Saturation behavior of the force gradient is illustrated as objects approach each other (dimensionless  $a$  decreasing). 1D: line-like objects, 2D: plate-like objects, 3D: point-like objects.

to compare the functions  $f_{\text{D}}[a]$ ; see Figure S3. For large separations, objects behave as if they are point-like particles (3D), but once the separation approaches the object’s major dimension, force gradients begin saturation. There is no saturation for the 3D case. The saturation is complete in the case of membranes (2D) — there is virtually no benefit in bringing two parallel membranes closer to each other than their major dimension. For the case of rods (1D), the improvement with respect to separation drastically decreases at the saturation point, nevertheless still showing some improvement.

Thus, the best strategy for an accurate comparison is to utilize the suitable geometry factor to calculate the force gradient at the separation point that the two objects touch — assuming that this dimension is larger than  $50 \mu\text{m}$ . As discussed in the main text, the closest approach of two objects will be limited to  $50 \mu\text{m}$ , as screening electromagnetic interactions to make gravity dominant below that level will not be meaningful.

### 3.2 Parameters used for $\eta$ comparisons

In Table S1, we tabulate the numbers utilized in the comparison for the  $\eta$  parameters for the different oscillators shown in Fig. 3. These are the numbers that go directly into Equation 1. Recall the geometric quantities used to calculate the force gradient  $|\nabla F|$ : the center separation between objects  $d$  and the major dimension of the object  $L$  — e.g., diameter of a sphere, side length of a square membrane, or length of a cantilever.

Osc.	$m$ (kg)	$f$ (Hz)	$x_{zp}$ (m)	$\xi$ (m)	${}^\dagger L$ (m)	${}^* d$ (m)
a)	$1.2 \times 10^{-18}$	$57 \times 10^3$	$1.1 \times 10^{-11}$	$2.5 \times 10^{-11}$	${}^{3D}100 \times 10^{-9}$	$50 \times 10^{-6}$
b)	$2.8 \times 10^{-18}$	$305 \times 10^3$	$3.1 \times 10^{-12}$	$2.3 \times 10^{-12}$	${}^{3D}140 \times 10^{-9}$	$50 \times 10^{-6}$
c)	${}^\ddagger 2.9 \times 10^{-15}$	$4.3 \times 10^6$	$2.6 \times 10^{-14}$	$7.6 \times 10^{-15}$	${}^{1D}65 \times 10^{-6}$	$50 \times 10^{-6}$
d)	$9.4 \times 10^{-13}$	63	$1.8 \times 10^{-15}$	$1.4 \times 10^{-15}$	${}^{3D}10 \times 10^{-6}$	$50 \times 10^{-6}$
e)	${}^\ddagger 2.3 \times 10^{-12}$	$1.1 \times 10^6$	$1.8 \times 10^{-15}$	$1.4 \times 10^{-15}$	${}^{2D}0.7 \times 10^{-3}$	$50 \times 10^{-6}$
f)	${}^\ddagger 14 \times 10^{-12}$	$274 \times 10^3$	$1.5 \times 10^{-15}$	$2.7 \times 10^{-16}$	${}^{1D}90 \times 10^{-6}$	$50 \times 10^{-6}$
g)	${}^\ddagger 43 \times 10^{-12}$	$705 \times 10^3$	$5.3 \times 10^{-16}$	$3.2 \times 10^{-16}$	${}^{2D}1.0 \times 10^{-3}$	$50 \times 10^{-6}$
h)	$5.6 \times 10^{-9}$	240	$2.5 \times 10^{-15}$	${}^1 1.2 \times 10^{-19}$	${}^{3D}0.1 \times 10^{-3}$	$0.1 \times 10^{-3}$
i)	${}^\ddagger 16 \times 10^{-9}$	$6.0 \times 10^9$	$3.0 \times 10^{-19}$	${}^2 2.1 \times 10^{-18}$	${}^{1D}0.4 \times 10^{-3}$	$50 \times 10^{-6}$
This	$1.0 \times 10^{-6}$	18	${}^3 1.2 \times 10^{-15}$	${}^3 1.2 \times 10^{-18}$	${}^{1D}2 \times 10^{-3}$	$0.5 \times 10^{-3}$
j)	$5.0 \times 10^{-6}$	662	$5.0 \times 10^{-17}$	$5.2 \times 10^{-20}$	${}^{2D}3.0 \times 10^{-3}$	${}^4 0.5 \times 10^{-3}$
k)	$1.0 \times 10^{-3}$	$1 \times 10^3$	$2.9 \times 10^{-18}$	$5.5 \times 10^{-21}$	${}^{2D}12 \times 10^{-3}$	${}^5 4.0 \times 10^{-3}$
l)	${}^\ddagger 10$	148	$7.5 \times 10^{-20}$	$1.6 \times 10^{-20}$	${}^{3D}0.35$	0.35
m)	${}^\ddagger 1.1 \times 10^3$	900	$2.9 \times 10^{-21}$	$3.3 \times 10^{-23}$	${}^{1D}3.0$	0.40

**Table S1: Numbers utilized for different oscillators for  $\eta$  comparison in Fig. 3.** Experiments: (a) nanosphere (42), (b) nanosphere (43), (c) nanobeam (44), (d) microsphere (45), (e) membrane (46), (f) cantilever (47), (g) membrane (48), (h) superconducting microsphere (12), (i) acoustic resonator (49), (j) pendulum (36), (k) pendulum (35), (l) LIGO pendulums (41), (m) bar resonator (50).

${}^\dagger$  Object's major characteristic dimension.

${}^*$  Smaller of the two: center separation when objects touch, or  $50 \mu\text{m}$  due to shielding arguments.

${}^{1D}$  Utilized geometry factor is  $f_{1D}$ .

${}^{2D}$  Utilized geometry factor is  $f_{2D}$ .

${}^{3D}$  Utilized geometry factor is  $f_{3D}$ .

${}^\ddagger$  These are effective masses provided by the respective references.

${}^1$  Based on lowest observed motional temperature of 2.5 K; private communication.

${}^2$  Coherence length calculated based on Schrodinger cat separation  $\bar{n} = 2.6$  with  $\xi = 4x_{zp} \sqrt{\bar{n} + \frac{1}{2}}$ .

${}^3$   $x_{zp} \equiv \theta_{zp} l$  and  $\xi \equiv \xi_\theta l$  are calculated based on pendulum lever arm of  $l = 1 \text{ mm}$ .

${}^4$  For pendulum dimensions refer to ref. (11).

${}^5$  Pendulum dimensions extracted from ref. (68).